nature communications

Article

https://doi.org/10.1038/s41467-025-58291-7

Second coordination sphere regulates nanozyme inhibition to assist early drug discovery

Received: 17 August 2024

Accepted: 17 March 2025

Yu Wu[1,4], Jian Li[1,4], Wenxuan Jiang[1], Weiqing Xu[1], Lirong Zheng[2], Canglong Wang[3], Wenling Gu[1] & Chengzhou Zhu[1] ✉

Early drug discovery is a time- and cost-consuming task requiring enzymes. Although nanozymes with metal sites akin to metallocofactors display similar activities, the lack of proximal amino acids hinders them from more adequately mimicking enzymes for drug discovery purposes. Hence, the rational design of the nanozyme second coordination sphere is desirable yet remains challenging. Herein, we report a nanozyme featuring atomically dispersed Cu-N_4 sites with proximal hydroxyl groups (CuNC-OH). Experimental and theoretical results reveal that Cu-N_4 site and hydroxyl respectively behave as cofactor and amino acid of the enzymatic pocket to interact with adsorbates, regulating nanozyme activity and inhibition. This mechanism involving dual sites is similar to that of thyroid peroxidases, which enables specific inhibition of CuNC-OH by antithyroid drugs. Based on these findings, a nanozyme-assisted drug discovery kit is established to analyze inhibition features of thyroid peroxidase inhibitors and screen out promising antithyroid drugs with a significant cost reduction compared with traditional enzyme kits.

Drug discovery is a complex process requiring a substantial commitment of time, money, and effort[1]. To effectively screen out candidate drugs, most strategies have been developed based on drug targets[2,3], such as enzymes, metabolites, receptors, and so on. The success in both clinics and businesses makes enzyme inhibitors become the major focus[4], which occupy approximately half of the drugs in the market. Facing various candidate molecules, the enzyme inhibition assay is carried out in the primary screen stage for identifying and classifying inhibitors possessing a specific mechanism. Notably, enzyme kinetic study is informative in the understanding of drug act yet restricted by some intrinsic drawbacks of native enzymes[5]. Due to the difficulty in separation and purification, obtainable enzymes are commonly expensive with poor yield and uneven quality, while more enzymes remain unavailable in the market. Moreover, the protein skeleton is susceptible to many environmental factors (e.g., temperature and pH) and the denaturation of enzymes increases costs and influences the reliability of assay results. Therefore, advanced alternatives to enzymes are anticipated to assist in early drug discovery.

As one of the state-of-the-art artificial enzymes, nanozymes have received great interest in various traditional enzymatic applications as the alternative to enzymes[6–8], such as pollutant degradation[9–11], therapy[12–15], and biosensing[16–18]. Inspired by the enzyme structure, attempts have been made to engineer atomic metal-nitrogen sites (M-N_x) akin to that of native metallocofactors[19–22], which successfully endow nanozymes with superior enzyme-like activities[23,24]. Nevertheless, most approaches neglect to equip the metal site with a properly designed second coordination sphere[25–27], as various amino acids surround the metallocofactor in the enzymatic pocket. Given the critical role of proximal amino acids in controlling the access to metallocofactors[28], most nanozymes with only exposed metal sites fail to mimic the specificity of native enzymes and further perform complex catalytic applications, including drug discovery. Thus, tailoring

---

[1]State Key Laboratory of Green Pesticide, International Joint Research Center for Intelligent Biosensing Technology and Health, College of Chemistry, Central China Normal University, Wuhan, PR China. [2]Beijing Synchrotron Radiation Facility, Chinese Academy of Science, Beijing, PR China. [3]Institute of Modern Physics, Chinese Academy of Science, Lanzhou, PR China. [4]These authors contributed equally: Yu Wu, Jian Li. ✉e-mail: czzhu@ccnu.edu.cn

the second coordination sphere of nanozymes is of great importance, which, however, is full of challenges for advancing their practical applications.

Herein, we report a class of nanozymes featuring Cu-N_4 sites with proximal hydroxyl groups (CuNC-OH) for assisting in the discovery of antithyroid drugs. The atomic structure akin to the heme of native peroxidases enables the expression of peroxidase-like activity. The specific activity *per* Cu-N_4 sites of CuNC-OH (343.92 M^{-1} min^{-1}) is 7.19 times higher than that of bare CuNC (47.82 M^{-1} min^{-1}). Mechanistic investigations reveal that the proximal hydroxyl group functions like an amino acid side chain to optimize the conformation of adsorbed H_2O_2 for activity enhancement. Moreover, proximal hydroxyl groups can regulate the binding to inhibitors, enabling CuNC-OH to exhibit different inhibition modes toward various mercapto inhibitors. Specifically, a similar spatial arrangement to the pocket of thyroid peroxidase endows CuNC-OH with a more specific binding strength toward antithyroid drugs. Finally, a nanozyme kit was designed to analyze inhibition features of different inhibitors, which is applicable to not only the primary screening of thyroid drugs in the early stage but also the quality analysis of commercial drugs.

Results

Typically, a salt-template strategy was employed to synthesize CuNC-OH (Fig. 1a). First, $Cu(NO_3)_2$, *o*-phenylenediamine (OPD), and KCl template were mixed in methanol. The obtained dry powders were further annealed under the nitrogen flow. After removing KCl with ultrapure water, the resultant samples were etched with sulfuric acid to remove aggregated Cu species and CuNC was obtained. Finally, CuNC-OH was prepared after treating CuNC with oxidative nitric acid. Transmission electron microscopy (TEM) images first show the ultrathin nanosheet structure of CuNC-OH and CuNC (Fig. 1b and Supplementary Fig. 1), where the treatment by nitric acid has negligible influences on the morphology of carbon supports. High-resolution TEM (HR-TEM) images reveal their amorphous crystalline without aggregated species (Supplementary Fig. 2), according well with X-ray diffraction patterns (Supplementary Fig. 3). High-angle annular dark-field scanning TEM (HAADF-STEM) together with energy dispersion spectroscopy (EDS) images indicate that all Cu, N, O, and C elements disperse evenly in two samples (Supplementary Fig. 4). Aberration-corrected HAADF-STEM was employed to visualize the dispersion of Cu atoms (Fig. 1c and Supplementary Fig. 5). Combining the intensity

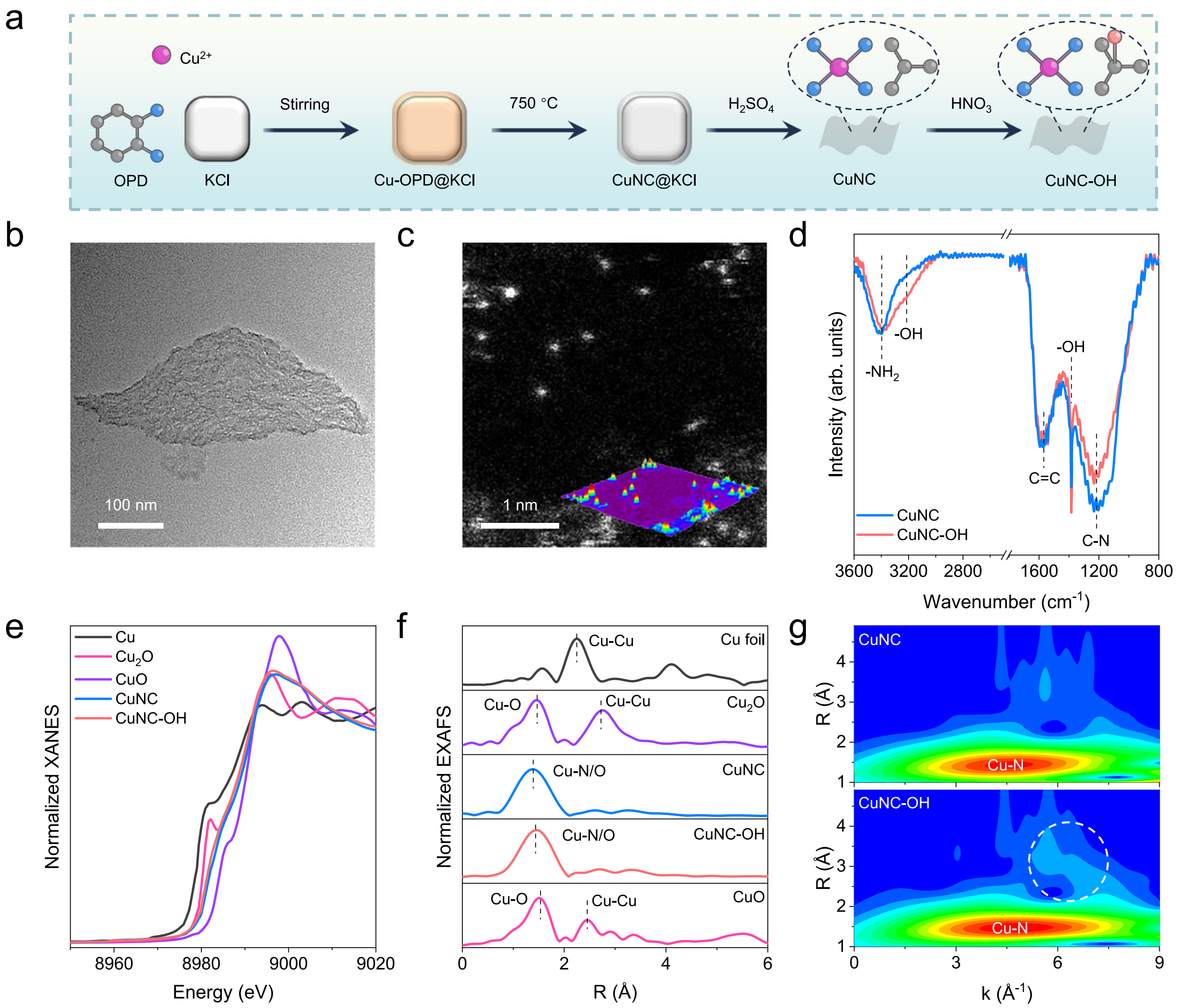

Fig. 1 | Synthesis and characterization. a Synthesis scheme of CuNC and CuNC-OH. **b** TEM and (**c**) AC-HAADF-STEM images of CuNC-OH. Inset: corresponding intensity profile of grayscales. **d** FTIR spectra of CuNC-OH and CuNC. **e** XANES and (**f**) EXAFS spectra of CuNC-OH, CuNC, and standard references. **g** WT-EXAFS of CuNC and CuNC-OH. Source data are provided as a Source Data file.

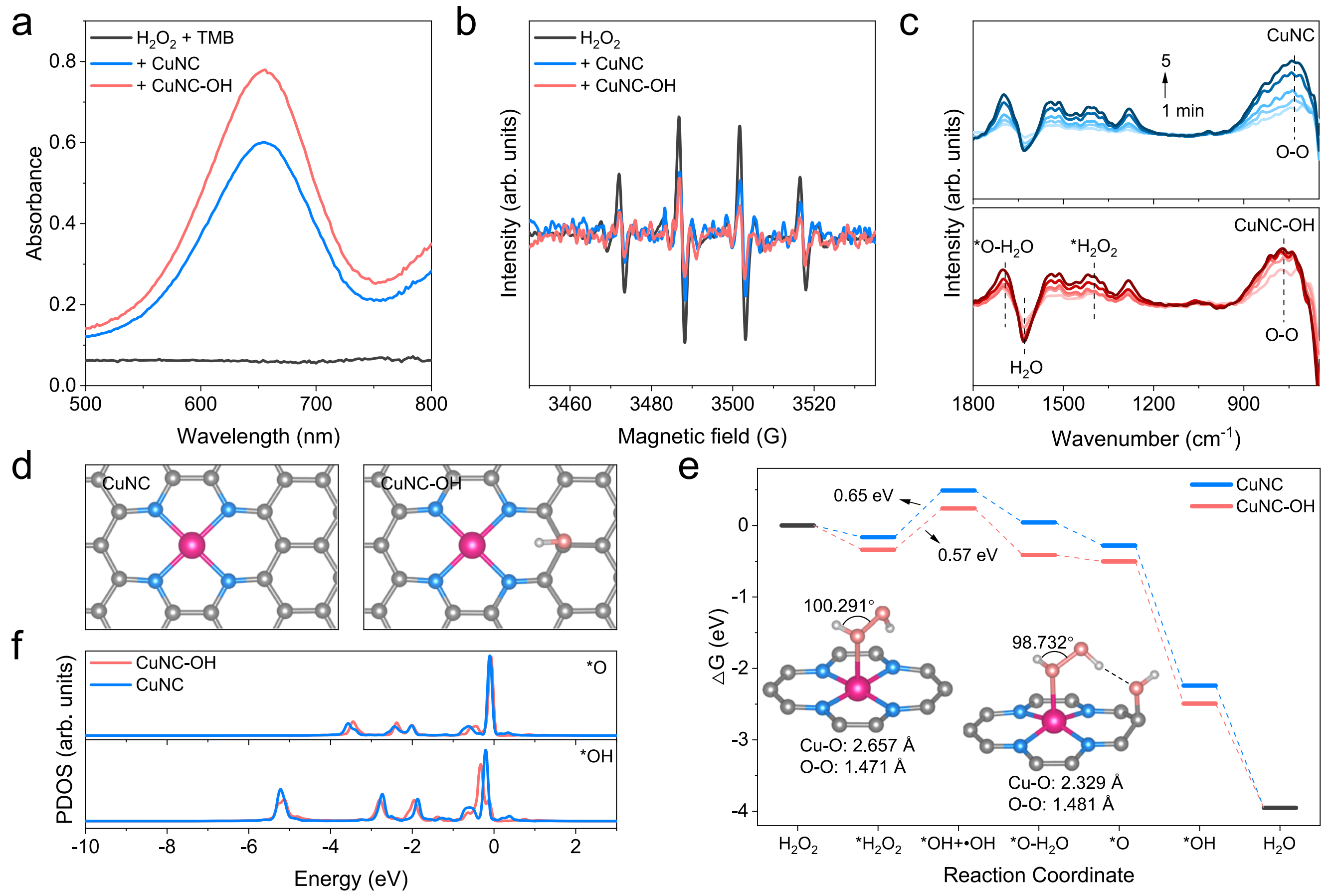

Fig. 2 | Characterization of the peroxidase-like activity. a Absorption spectra of H_2O_2 + TMB in the absence and presence of CuNC and CuNC-OH, respectively. **b** EPR spectra with DMPO trapping agent of H_2O_2, H_2O_2 + CuNC, and H_2O_2 + CuNC-OH. **c** Time-dependent in situ FTIR spectra of H_2O_2 + CuNC and H_2O_2 + CuNC-OH. **d** Theoretical models of CuNC and CuNC-OH. **e** Energy profiles of CuNC and CuNC-OH for peroxidase-like activity. Insets are the optimized models of adsorbed H_2O_2 on CuNC and CuNC-OH, respectively. Cu: amaranth; N: blue; C: gray; O: pink; H: white. **f** PDOS plots for O *p* states of *O and *OH of CuNC-OH and CuNC. Source data are provided as a Source Data file.

profile, abundant isolated bright dots demonstrate the atomic dispersion of Cu sites. The Cu loading of CuNC and CuNC-OH was further determined by inductively coupled plasma optical emission spectroscopy (ICP-OES) as 0.89 wt% and 0.74 wt%, respectively. The Fourier transform infrared (FTIR) spectroscopy was performed to characterize the carbon support (Fig. 1d). In comparison, CuNC-OH possesses an increased -OH signal at 3210 and 1383 cm^{-1}, indicating that nitric acid with strong oxidability introduces more -OH in the carbon support. Correspondingly, X-ray photoelectron spectroscopy (XPS) confirms the increased O content in CuNC-OH (9.30 at%) in comparison to CuNC (7.42 at%) (Supplementary Fig. 6 and Supplementary Table 1). In comparison, the shift of O *1 s* to the high binding energy is assigned to the increase of -OH peak (Supplementary Fig. 7), while the contents of other oxygen species are not affected. Moreover, Zeta potential analysis shows an opposite result of CuNC-OH (−35.5 mV) from that of CuNC (9.1 mV), which can be well explained by implantation of -OH (Supplementary Fig. 8).

X-ray absorption spectroscopy was subsequently carried out to study the electronic structure of CuNC-OH. As expected, In the Cu K-edge X-ray absorption near edge structure (XANES) spectra (Fig. 1e), the adsorption edge of CuNC-OH is located nearly to that of CuNC, indicating the electronic structure of Cu is not affected by the introduction of -OH. In comparison to Cu_2O and CuO references, the valence state of Cu is +1 ~ +2[29]. Extended X-ray absorption fine structure (EXAFS) further provides the coordination information of Cu sites at the atomic level. As shown in Fig. 1f, the prominent peak approximately at 1.40 Å observed in two samples can be assigned to the Cu-N coordination by contrasting to referring Cu_2O and CuO[30]. Moreover, the lack of the Cu-Cu path further reveals that Cu sites disperse atomically. According to fitted EXAFS results (Supplementary Fig. 9), Cu sites of CuNC-OH (3.79 and 1.95 Å) share a similar coordination structure with that of CuNC (3.96 and 1.94 Å) (Supplementary Table 2). Likewise, the same signal maximums at ~4.5 Å^{-1} emerging in wavelet-transformed (WT) EXAFS spectra of two CuNC verify the Cu-N primary coordination (Fig. 1g). The difference at ~7.0 Å^{-1} further confirms the changed second coordination sphere of CuNC-OH, where the R-value range (3.5–4.0 Å) indicates the approximate distance between Cu and proximal hydroxyl.

The peroxidase-like activity was tested using the classic colorimetric regent 3,3',5,5'-tetramethylbenzidine (TMB)[31–33], and the oxidized production of TMB possesses a typical absorption maximum at 652 nm (Fig. 2a). According to kinetic experiments (Supplementary Fig. 10), CuNC-OH with a low Michaelis constant (K_m) of 41.30 mM shows superior H_2O_2 affinity to CuNC (69.36 mM) (Supplementary Table 3). Furthermore, the specific activity *per* Cu sites of CuNC-OH (343.92 M^{-1} min^{-1}) is about 7.19 times higher than that of CuNC (47.82 M^{-1} min^{-1}). To explore the catalytic processes of CuNC-OH, electronic paramagnetic resonance (EPR) and in situ attenuated total reflection Fourier transform infrared (ATR-FTIR) spectroscopy were performed to probe the active intermediates produced in the catalysis. Using 5,5-dimethyl-1-pyrroline N-oxide (DMPO) as the spin-trapping agent (Fig. 2b), the typical signals of the •DMPO-OH adduct indicate the existence of hydroxyl radicals (•OH). However, the signal intensity is reduced in the presence of CuNC-OH and CuNC, which means the common H_2O_2 homolysis mechanism of nanozymes is not applicable here. According to in situ ATR-FTIR spectra (Fig. 2c), similar variations observed in CuNC-OH and CuNC reveal that the second coordination sphere does not influence the catalytic routine of Cu-N_4 sites. The increases of OOH bending at 1390 cm^{-1} indicate the H_2O_2 adsorption[34]. Notably, the O-O peak (767 cm^{-1}) of CuNC-OH shifts to the high wavenumber relative to that of CuNC (730 cm^{-1}), which can be attributed to the impact of proximal hydroxyl on adsorbed peroxide species[35]. Furthermore, increasing signals at 1680 cm^{-1} reveal the formation of *O-H_2O intermediates[36]. Notably, native copper-dependent enzymes follow a Fenton-type H_2O_2 activation rather than the heterolysis mechanism involved in some heme peroxidases[37]. As depicted in Supplementary Fig. 11, Cu sites first prompt the homolysis of O-O bonding, where the produced transient •OH readily induces the hydrogen atom abstraction (HAA) from the other intermediate Cu-OH and finally forms *O-H_2O. Given the consumption of •OH and the production of *O-H_2O observed above, this mechanism can be applied to describe the catalytic processes of CuNC-OH and CuNC.

Theoretical calculations based on density functional theory (DFT) were further carried out to understand the influences of the second coordination sphere on the peroxidase-like activity of CuNC-OH. CuNC was first modeled using a Cu-N_4 doped graphene (Fig. 2d), where the Cu-N distance of 1.93 Å matches well with the fitted EXAFS results of 1.94 Å. Subsequently, the carbon site neighbor to Cu-N_4 sites was modified with -OH to serve as the model of CuNC-OH. In comparison with other possible models (Supplementary Fig. 12), its Cu-N_4 site is slightly affected by the proximal hydroxyl, and both Cu-N (~1.95 Å) and Cu-O (3.91 Å) distances are consistent with EXAFS results. The catalytic profiles of CuNC and CuNC-OH were further investigated (Fig. 2e). First, the Cu-N_4 site binds with H_2O_2 to obtain *H_2O_2 (Supplementary Fig. 13). For CuNC-OH, proximal -OH can interact with H_2O_2 via hydrogen bond, resulting in a more significant Gibbs energy change (ΔG) of −0.34 eV than that of CuNC (−0.16 eV). Notably, adsorbed H_2O_2 on CuNC-OH presents a prolonged O-O length, a shortened Cu-O length, and a reduced H-O-OH angle. These changes are beneficial to the interaction between H and OH, where the •OH produced in the subsequent Fenton-type activation more readily induces the HAA and further produces *O-H_2O. As expected, CuNC needs to overcome a higher energy cost of 0.65 eV than CuNC-OH (0.57 eV). More importantly, the activation serves as the rate-determining step, explaining that the superior activity of CuNC-OH originates from the enhanced H_2O_2 activation. The following step of H_2O desorption is thermodynamically favorable in both CuNC-OH and CuNC. Finally, *O is sequentially reduced into *OH and H_2O, accompanied by the oxidation of two TMB molecules. The partial density of states (PDOS) analysis was employed to study the reactivity of active *O and *OH intermediates (Fig. 2f). In comparison, similar p states of O indicate the reactivity of *O remains the same in two nanozymes, which is also reflected by the similar Cu-O lengths (Supplementary Fig. 14). Likewise, the reactivity of *OH is weakly affected by the proximal hydroxyl. Based on the analysis above, the proximal hydroxyl in the second coordination sphere boosts the peroxidase-like activity of Cu-N_4 sites by improving the adsorption and activation of H_2O_2 rather than directly affecting the structure of Cu-N_4 sites, which is similar to the function of amino acid residue in the enzymatic pocket.

Due to the strong interaction between thiol and metal, mercapto molecules, like cysteine (Cys), are widely reported as nanozyme inhibitors yet being unselectively[38,39]. For enzyme inhibitors with higher specificity, interactions with proximal amino acid residues are also important. Typically, methimazole (MMI) as an antithyroid drug targets the thyroid peroxidase[40,41], wherein the S atom can coordinate with metal sites while imidazole forms a hydrogen bond with histidine in the second coordination sphere (Fig. 3a). Inspired by this, MMI and Cys as two model inhibitors were used to explore the function of second coordination spheres in regulating inhibition. XPS spectra on O *1s* of CuNC-OH with an obvious shift (−0.36 eV) of -OH first reveal its electron loss upon the inhibition by MMI (Supplementary Fig. 15). In comparison, peaks of CuNC are weakly affected, confirming the shift is induced by the interaction between inhibitors and the second coordination sphere. In addition, a peak at 167.4 eV emerging in XPS on S *2p* can support that the reducibility of thiols also induces the inhibition (Supplementary Fig. 16). Furthermore, kinetic experiments reveal that CuNC is significantly inhibited by both inhibitors (Fig. 3b), while CuNC-OH presents a more specific inhibition behavior by MMI. Based on the Michaelis-Menten equation, variations of the maximum reaction velocity (V_{max}) and K_m further reveal the different inhibitory effects of MMI and Cys (Fig. 3c). For this redox system catalyzed by metal sites, both the reducibility and coordination ability of thiols can induce the inhibition of peroxidase-like activity[42]. In the presence of MMI, both V_{max} and K_m of CuNC-OH decrease at almost the same rate, revealing that the uncompetitive inhibition is dominating (Supplementary Note 1)[43]. However, V_{max} and K_m of CuNC follow different variation rates, verifying the existence of more inhibition modes besides uncompetitive inhibition. Given the sole Cu-N_4 binding site, the loose adsorption of MMI may cause this complex inhibition mode, and the type of other modes is difficult to be verified. In contrast, the proximal hydroxyl in CuNC-OH is considered to synergize with the Cu-N_4 site for adsorbing MMI in a more stable conformation, reflected by its single uncompetitive inhibition mode. A more complicated inhibition occurs when using Cys as the inhibitor. The decreased V_{max} of CuNC is assigned to the competitive inhibition (Supplementary Note 2), while increased K_m originates from the non-competitive inhibition (Supplementary Note 3). The coexistent multiple inhibition modes are explained by the lack of second coordination spheres as well. While for CuNC-OH, the inhibition of Cys is weak. Given that Cys contributes a lot in maintaining redox balance redox in vivo[44], the reducibility of Cys is responsible for the minor change of K_m (Supplementary Note 4). Therefore, CuNC-OH with a superior peroxidase-like activity can quickly consume Cys. As a result, the non-competitive inhibition of Cys is also weakened, further explaining the minor decrease of V_{max}.

DFT calculations further demonstrate the critical role of proximal hydroxyl in enhancing the adsorption of MMI. Similar to the conformation of MMI adsorbed in thyroid peroxidase, the thiol and imidazole of MMI interact with the Cu-N_4 site and -OH of CuNC-OH, respectively (Supplementary Fig. 17). With the assistance of -OH, the Cu-S distance is shortened from 2.352 Å of CuNC to 2.326 Å of CuNC-OH. Further comparing the adsorption energy (ΔE), the stronger adsorption toward MMI than H_2O_2 by both nanozymes explains the inhibition phenomena (Fig. 3d), where the ΔE differences of CuNC-OH (0.78 eV) and CuNC (0.68 eV) further correspond to their inhibition levels. According to the differential charge density (DCD) analysis (Fig. 3e), S atoms of two *MMI models present similar changes in electronic structures with almost the same Mulliken charges (-0.376 and −0.373), indicating the Cu-S interaction contributes equally to the adsorption of MMI in the two models. Meanwhile, the Mulliken charge of the hydroxyl O atom changes from −0.396 to −0.473, supporting the electron loss in the XPS characterizations above. The imidazole H atom of *MMI on CuNC-OH shows a decreased electron density and a more positive Mulliken charge (0.298), attributing to the interaction with proximal hydroxyl. In comparison, the electronic structure of the imidazole H atom of *MMI on CuNC (0.244) is close to that of free MMI (0.241) (Supplementary Fig. 18). Hence, the boosted adsorption of MMI is attributed to the function of the second coordination sphere.

The mechanism of action of antithyroid drugs, including MMI, is mainly attributed to their inhibitory effect on thyroid peroxidase, where thiol groups can not only block the metal center but also reduce oxidative intermediates[41]. Based on this protocol, the enzyme-based drug discovery kit (EDDK) is employed in the drug primary screen stage to obtain the inhibition features of various molecules and find drug candidates (Fig. 4a). However, the high cost of enzymes becomes

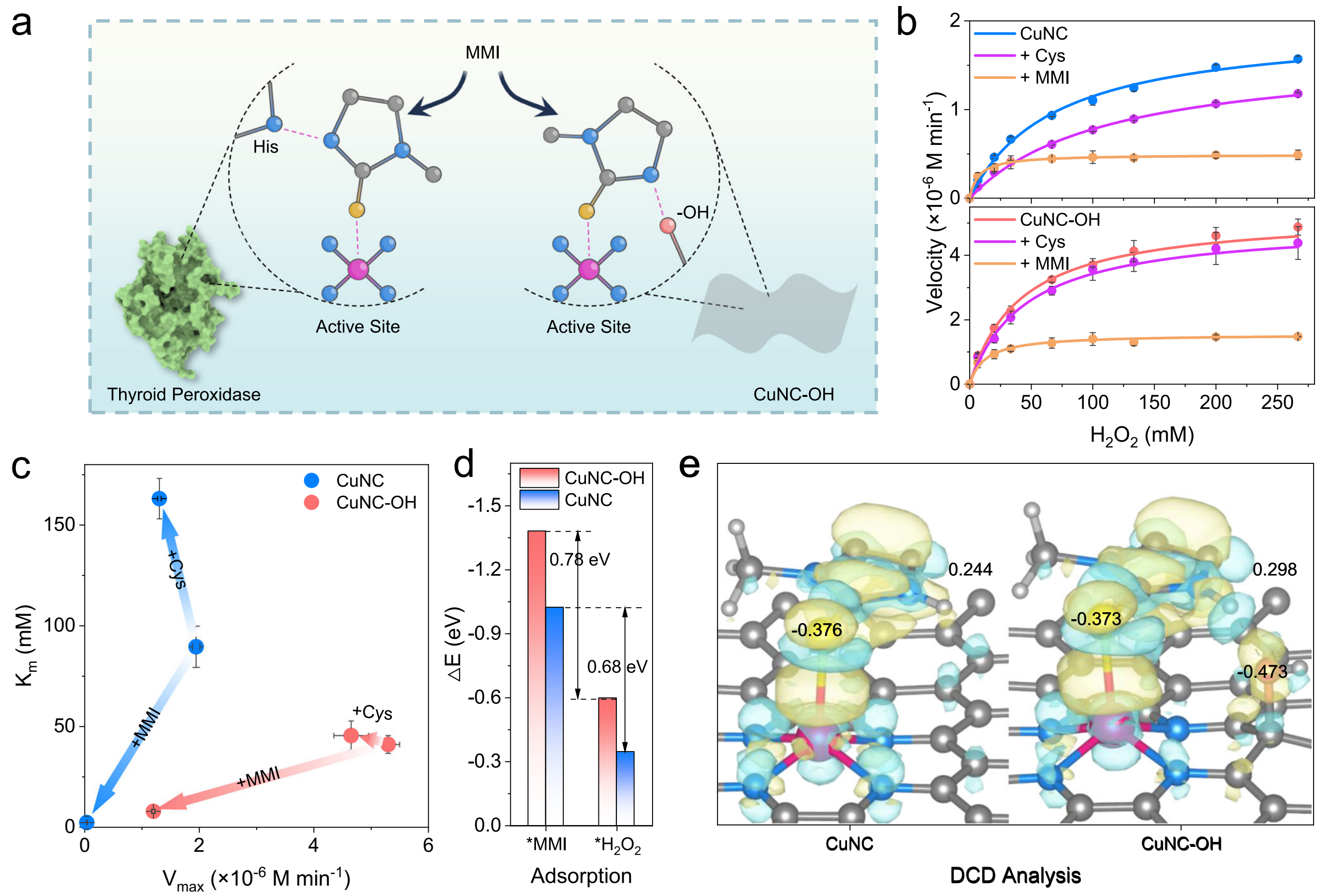

Fig. 3 | Inhibition of peroxidase-like activity. a Scheme of MMI adsorption in thyroid peroxidase and CuNC-OH, respectively. **b** Kinetic experiments and (**c**) K_m and V_{max} of CuNC and CuNC-OH in the absence and presence of different inhibitors (33.33 µM). The error bars correspond to the standard deviation of at least three independent measurements. **d** Adsorption energy of CuNC and CuNC-OH for MMI and H_2O_2 adsorption, respectively. **e** DCD analysis of *MMI on CuNC and CuNC-OH. Light yellow regions represent the electron accumulation and light blue regions represent the electron consumption. Cu: amaranth; N: blue; C: gray; O: pink; H: white; S: yellow. Inset: Mulliken charges of S and H atoms. Source data are provided as a Source Data file.

the main limitation since a large consumption of enzymes is required for abundant drug candidates. To address this issue, we achieved a nanozyme-assisted drug discovery kit (NDDK). Specifically, by using existing drugs as the internal reference, NDDK can recognize those molecules with similar inhibition features, which can be subsequently confirmed by enzymes with a reduced dosage. For high-throughput screening with fewer operating errors, a microfluidic chip was further established to efficiently perform experiments (Fig. 4b). The microfluidic chip is composed of a body with channels, a cap, and two valves (Supplementary Fig. 19), where CuNC-OH and CuNC are immobilized to drive the chip. Specifically, CuNC-OH with enhanced peroxidase-like activity and inhibitor specificity can well reflect the inhibition of antithyroid drugs, while CuNC can also provide information on the inhibition toward Cu-N_4 sites. Scanning electron microscopy (SEM) images show that 3–5 layers of nanosheets stack loosely on the chip with sufficiently exposed surfaces (Supplementary Fig. 20), enabling subsequent interactions with either substrates or inhibitors. To operate the chip, the drug analyte is first put in as depicted in Fig. 4c, which is subsequently brought by the buffer to CuNC-OH and CuNC for inhibition. After spinning valves to switch channels, H_2O_2 and TMB are introduced for catalysis, where color signals can be further collected in two semicircular regions.

As proof of concept, NDDK was performed on several commercial antithyroid drugs, including MMI, propylthiouracil (PTU), methylthiouracil (MTU), carbimazole (CBZ). Notably, many other mercapto drugs also utilize the coordination ability and reducibility of thiols for therapy[45], which were included as invalid antithyroid drug models. Also, inhibitors with other forms of sulfur were introduced, and the sulfur-free molecule of ascorbic acid (AA) was employed as a control inhibitor with reducibility. Detailed structures of these inhibitors (labeled from a-n) can be found in Supplementary Fig. 21. After determining their inhibition features, the principal component analysis (PCA) was used to reduce dimensionality. Subsequently, a classic machine learning algorithm, support vector machine (SVM), was performed for the classification (Fig. 4d). The SVM decision region boundary successfully classifies antithyroid drugs and other molecules. The high prediction accuracy can be supported by the confusion matrix (Fig. 4e). Notably, the results of four antithyroid drugs tend to aggregate in the SVM plot owing to their similar inhibition features. Inspired by this phenomenon, NDDK is promising in the primary screening of antithyroid drugs by finding similar inhibition features. The blind tests were carried out to verify the feasibility, where more samples (labeled from 0-9) possessing similar structures to MMI and PTU were tested (Supplementary Fig. 22). Consequently, benzylthiouracil (BTU) and captopril were screened, and other multiple inhibitors were weeded out. Notably, BTU serves as another antithyroid drug in the market, and captopril is reported to inhibit iodination reactions by thyroid peroxidase[46]. These results can prove the satisfying performance of NDDK in the primary screening stage of drug discovery. In comparison with EDDK, the test of the above molecules using NDDK can achieve a significant cost reduction of approximately 1966.88 $, owing to the low cost of CuNC-OH (~0.0085 $ mg^{-1}). In addition, NDDK can be employed for the quality assay in drug discovery (Supplementary Fig. 23). Within the MMI concentration range

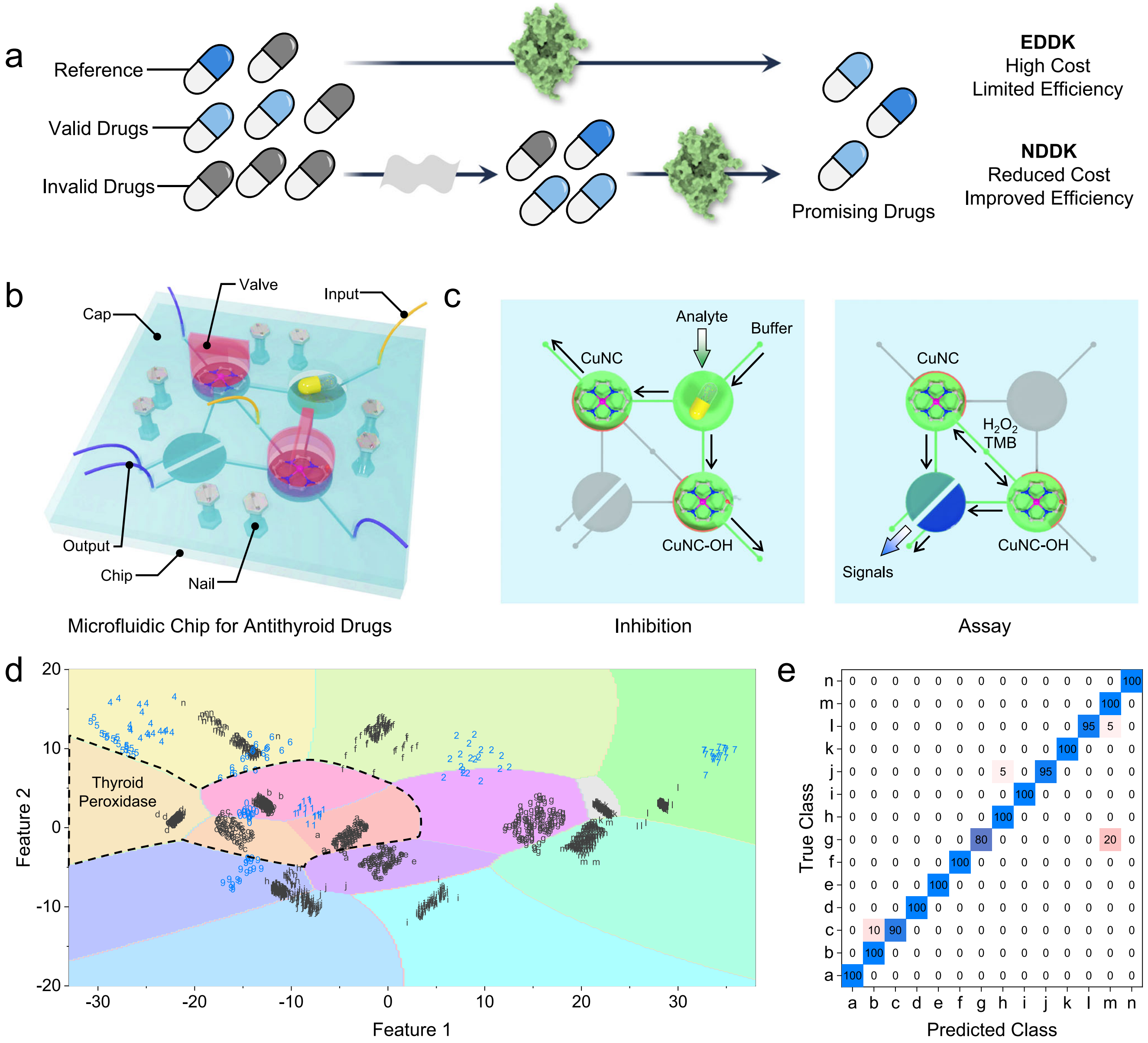

True Class	a	b	c	d	e	f	g	h	i	j	k	l	m	n
n	0	0	0	0	0	0	0	0	0	0	0	0	0	100
m	0	0	0	0	0	0	0	0	0	0	0	0	100	0
l	0	0	0	0	0	0	0	0	0	0	0	95	5	0
k	0	0	0	0	0	0	0	0	0	0	100	0	0	0
j	0	0	0	0	0	0	0	5	0	95	0	0	0	0
i	0	0	0	0	0	0	0	0	100	0	0	0	0	0
h	0	0	0	0	0	0	0	100	0	0	0	0	0	0
g	0	0	0	0	0	0	80	0	0	0	0	0	20	0
f	0	0	0	0	0	100	0	0	0	0	0	0	0	0
e	0	0	0	0	100	0	0	0	0	0	0	0	0	0
d	0	0	0	100	0	0	0	0	0	0	0	0	0	0
c	0	10	90	0	0	0	0	0	0	0	0	0	0	0
b	0	100	0	0	0	0	0	0	0	0	0	0	0	0
a	100	0	0	0	0	0	0	0	0	0	0	0	0	0

Fig. 4 | Application for primary screening of antithyroid drugs. a Protocols of the primary screen by EDDK and NDDK. **b** Schematic compositions of microfluidic chip. **c** Schematic illustrating operation protocols. **d** Decision region boundary plot obtained from SVM for recognizing inhibitors. **e** Confusion matrix of the predicted class and true class when recognizing different inhibitors. Source data are provided as a Source Data file.

of 16.67–120.00 μM, two linear curves of CuNC-OH and CuNC can collectively quantify the content of MMI (Supplementary Table 4). Likewise, the assay of PTU can be successfully achieved. By applying NDDK to analyze commercial tablets, the active ingredient concentration detected is close to the labeled amounts (Supplementary Table 5), where the difference may be attributed to the interference from coexistent additives. Moreover, those degenerative commercial tablets upon simulated stimuli can be recognized by monitoring the variation of inhibitions to avoid health problems (Supplementary Fig. 24). In short, by employing NDDK as a supporting tool in the primary screening stage and quality tests of drug discovery, the consumption of enzymes can be effectively reduced to achieve a significant cost saving.

Discussion

In summary, this study creates a CuNC-OH nanozyme with the engineered second coordination sphere to assist early drug discovery. We revealed that proximal hydroxyl behaves as the natural amino acid of enzymatic pocket to contribute to the adsorption on Cu-N_4 sites. This interaction can efficiently optimize the conformation of adsorbed H_2O_2 to boost subsequent activation for the 7.19 times higher peroxidase-like activity. Moreover, the pocket arrangement is similar to that of native thyroid peroxidase, endowing CuNC-OH with a more specific binding strength toward antithyroid drugs. Taking advantage of the nanozyme inhibition regulation, an assay kit NDDK is developed to quantify the inhibitory effects of various molecules. Combining the machine learning algorithm, NDDK can assist in the primary screen of antithyroid drugs with a significant cost reduction. Moreover, NDDK is capable of monitoring the variation of inhibition for subsequent quality assay of commercial tablets. Our work attaches great importance to nanozyme inhibition and highlights the role of second coordination sphere design, and the attempt whereafter in drug discovery can set an example to broaden the application of nanozymes.

Methods

Materials

All the chemicals were used as received without further purification. $Cu(NO_3)_2{\cdot}3H_2O$, OPD, KCl, H_2SO_4, HNO_3, H_2O_2, methanol, ethanol, sodium acetate, and acetic acid were from Sinopharm Chemical Reagent Co. Ltd. (Shanghai, China). DMPO, TMB, Cys, GSH, and all drugs were from Aladdin Company. Commercial MMI tablets were from Merck. Commercial PTU tablets were from Wanbang Biopharmaceuticals. All the chemical reagents obtained are of analytical reagent grade.

Characterizations

TEM images were from Titan G2 F30 S-TWIN (Thermo Fisher, USA). XPS measurements were performed by ESCALAB 250Xi (Thermo Fisher, USA). XRD characterization was carried out by a D8 ADVANCE (Bruker, Germany). All UV−visible spectra were obtained via a multimode reader (Tecan Spark, Switzerland). Electron paramagnetic resonance (EPR) spectra were from Bruker A300. In situ ATR-FTIR analysis was performed using a Nicolet iS50 FT-IR spectrometer (Thermo) equipped with a diamond internal reflection element (IRE) (refractive index n diamond = 2.4, incidence angle $r = 42°$). A Milli-Q purification system (Millipore, MA) was used to obtain ultrapure water.

Synthesis of CuNC-OH and CuNC

Typically, $Cu(NO_3)_2{\cdot}3H_2O$ (0.07 g) and KCl (40 g) were mixed in methanol (30 mL), where OPD (0.08 g) was added subsequently. After stirring for 2 h, the precursor powder Cu-OPD@KCl was obtained through a drying process at 80 °C overnight. Then, Cu-OPD@KCl was annealed under N_2 flow (750 °C, 5 °C min^{-1}). Using H_2O to remove KCl template, the resultant samples were further etched by H_2SO_4 (1 M) to remove aggregated Cu species and prepare CuNC. Further treating CuNC with HNO_3 (1 M), CuNC-OH can be synthesized. The cost of CuNC-OH was calculated as 0.0085 \$ mg^{-1} according to the price of precursors.

Characterization of peroxidase-like activity

The H_2O_2-TMB system was used to characterize the peroxidase-like activity of CuNC-OH and CuNC. Specifically, 10 μL CuNC-OH suspension (0.1 mg mL^{-1}), 150 μL acetate buffer solution (0.1 M, pH = 3.5), 100 μL H_2O_2 (100 mM) and 50 μL TMB (1 mM dissolved in ethanol) were incubated at room temperature. The absorbance at 652 nm was recorded for further comparison.

Kinetic experiments

All the assays were conducted in acetate buffer (0.1 M, 150 μL, pH 3.5) at room temperature. Typically, CuNC-OH suspension (10 μL, 0.5 mg mL^{-1}), H_2O (50 μL), different concentrations of H_2O_2 solution (50 μL), and TMB (50 μL, 10 mM dissolved in ethanol) were added in sequence. The absorbance at 652 nm was recorded with the interval of 10 s, which was fitted linearly to obtain the initial velocity. Then, the initial velocity was plotted versus the concentration of H_2O_2 and further fitted by the nonlinear regression following the Michaelis-Menten equation:

$$1/V = K_m/(V_{\max}[S]) + 1/V_{\max} \quad (1)$$

where V is the initial velocity, [S] is the concentration of the substrate, K_m is the Michaelis-Menten constant, and V_{max} is the maximal reaction velocity.

To compare CuNC-OH and CuNC, the catalytic constant (k_{cat}) can be calculated by the following equation:

$$k_{cat} = V_{\max}/c \quad (2)$$

where c is the molar concentration of Cu sites.

Kinetic experiments with inhibitors

Similar to natural peroxidases, the peroxidase-like activity of CuNC-OH and CuNC is mainly from the activation of H_2O_2. Therefore, the inhibited kinetics toward H_2O_2 are studied in this section. The catalysis condition is similar to the parameters stated above, except for replacing H_2O (50 μL) with the Cys/MMI solution (50 μL, 0.05–0.4 mM). Other procedures are the same as stated above, where V_{max} and K_m were respectively plotted versus the concentration of mercapto inhibitors to study the activity inhibition.

DFT calculations

All spin polarization calculations were carried out using the $DMol^3$ code[47]. The electron interactions were described by Perdew-Burke-Ernzerhof (PBE) exchange-correlation functional within the generalized gradient approximation (GGA)[48]. The empirical correction in Grimme's scheme (DFT + D) was utilized to treat the Vander Waals interactions[49]. The double numerical plus polarization (DNP) basis set was used for other elements. Self-consistent field (SCF) computations were performed with the SCF tolerance of 10^{-6} on the total energy and electronic computations. Moreover, the real-space global orbital cutoff radius was chosen as high as 5.2 Å in all the computations. The Brillouin zone was sampled with a Monkhorst-Pack mesh with a 5 × 5 × 1 grid in reciprocal space during geometry optimizations. The vacuum space was set as 20 Å to avoid the interactions between periodic images.

The Gibbs free energy change (ΔG) of every elemental step was determined by the following equation: $\Delta G = \Delta E + \Delta ZPE - T\Delta S$. The reaction energy ($\Delta E$) can be directly determined by analyzing the DFT total energies. ΔZPE and ΔS are the zero-point energy difference and the entropy difference between the adsorbed state and the gas phase, respectively, and T is the system temperature (298.15 K). For each system, its ZPE can be calculated by summing vibrational frequencies overall normal modes υ ($ZPE = 1/2\sum\hbar\upsilon$). The entropies of the free molecules (H_2O_2, H_2, and H_2O) were taken from the NIST database, while the energy contribution from the adsorbed state was neglected. One-half of the chemical potential of H_2 molecule was used as the chemical potential of the proton-electron pairs. The free energy of •OH can be calculated in terms of the free energies of H_2O and H^+ according to the equation: $G(H_2O) = G(\bullet OH) + G(H^+) + E(-2.73\ V)$.

Preparation of the microfluidic chip

The microfluidic chip is prepared by a 3D print machine (UnionTech). To immobilize CuNC-OH onto the chip, the suspension (50 μL, 0.1 mg mL^{-1}) is mixed with 5% Nafion and dropped on the chip. After drying at 60 °C for 4 h, CuNC is immobilized using the same protocol. Subsequently, the chip is assembled using nails and reinforced by Vaseline to avoid leakage. Different solutions were respectively introduced into the chip through a pump with a flow rate of 1 ml min^{-1}.

Assay of drugs

The assay of different drugs was carried out using the resultant microfluidic chip. First, drug molecules (50 μL, 4 mM) were introduced into the chip. By injecting acetate buffer solution (0.1 M, pH = 3.5), drug molecules were brought to inhibit CuNC-OH and CuNC, respectively. After switching valves, H_2O_2 (100 mM) and TMB (1 mM dissolved in ethanol) were further injected for an incubation of 15 min. The absorbance at 652 nm (A_I) was recorded for further calculations. Similarly, blank signals were determined in the absence of drugs, which are denoted as A_0. The inhibition rate of a specific drug is calculated using $(1 - A_I/A_0) \times 100\%$. Finally, inhibition rates obtained from CuNC-OH and CuNC were collected for further analysis.

Blind tests using NDDK

To evaluate the efficiency of NDDK, 10 molecules with structures similar to MMI or PTU were tested. Python (version 3.13) was utilized for classification and prediction. Python libraries that support data processing and analysis include pandas (version 2.2.3), numpy (version 2.1.3), scikit-learn (version 1.5.2), and joblib (version 1.4.2). Seaborn (version 0.13.2) and matplotlib (version 3.9.2) were used to generate plots. Data standardization was performed using StandardScaler, followed by feature selection through PCA. The dataset was partitioned into training and test sets using an 80/20 split with stratified sampling to ensure consistent class distributions and a fixed random state was used for reproducibility. The SVM with an Radial Basis Function (RBF) kernel was used as the supervised classification model[50]. Model performance was further analyzed through confusion matrices along with standard evaluation metrics such as accuracy, precision, recall, and F1-score.

Cost of EDDK and NDDK

Notably, thyroid peroxidase is not sold in the market anymore, where the difficult acquisition of enzymes is one important cause for the design of NDDK. Given that the operation of NDDK is basically the same as that of EDDK, the cost difference is mainly attributed to the difference between thyroid peroxidase and CuNC-OH/CuNC. By referring to a former selling price of thyroid peroxidase (Aladdin T572858-1mg 2622.54 \$ mg^{-1}), the single test of 25 molecules in this work following procedures above requires about 1966.91 \$, while NDDK only consumes 0.026 \$.

Quality assay of commercial tablets

Before the assay, commercial tablets were ground into powers for dissolution. The powders were respectively treated with H_2O (1 mL), H_2O_2 (100 mM, 1 mL), ethanol (1 mL), 80 °C, and UV light. Subsequently, the assay was achieved based on the same protocols stated above.

Data availability

The data generated in this study are provided in this paper, its Supporting Information file, Source Data and from corresponding author upon request. Source data are provided with this paper.

Code availability

The source codes of this work are publicly available on GitHub at https://github.com/L0J1/SVM_CuNC_Drug and co-deposited on Zenodo at https://doi.org/10.5281/zenodo.15003366[50].

References

1. Hughes, J. P., Rees, S., Kalindjian, S. B. & Philpott, K. L. Principles of early drug discovery. *Brit. J. Pharmacol.* **162**, 1239–1249 (2011).
2. Imming, P., Sinning, C. & Meyer, A. Drugs, their targets and the nature and number of drug targets. *Nat. Rev. Drug Discov.* **5**, 821–834 (2006).
3. Chen, A. Y. et al. Targeting metalloenzymes for therapeutic intervention. *Chem. Rev.* **119**, 1323–1455 (2019).
4. Holdgate, G. A., Meek, T. D. & Grimley, R. L. Mechanistic enzymology in drug discovery: a fresh perspective. *Nat. Rev. Drug Discov.* **17**, 115–132 (2018).
5. Swinney, D. C. Biochemical mechanisms of drug action: what does it take for success? *Nat. Rev. Drug Discov.* **3**, 801–808 (2004).
6. Huang, Y., Ren, J. & Qu, X. Nanozymes: classification, catalytic mechanisms, activity regulation, and applications. *Chem. Rev.* **119**, 4357–4412 (2019).
7. Wu, Y. et al. Nanobiocatalysis: a materials science road to biocatalysis. *Chem. Soc. Rev.* **51**, 6948–6964 (2022).
8. Wu, J. et al. Nanomaterials with enzyme-like characteristics (nanozymes): next-generation artificial enzymes (II). *Chem. Soc. Rev.* **48**, 1004–1076 (2019).
9. Zhang, S. et al. Depolymerization of polyesters by a binuclear catalyst for plastic recycling. *Nat. Sustain.* **6**, 965–973 (2023).
10. Mondloch, J. E. et al. Destruction of chemical warfare agents using metal–organic frameworks. *Nat. Mater.* **14**, 512–516 (2015).
11. Zandieh, M. & Liu, J. Removal and degradation of microplastics using the magnetic and nanozyme activities of bare iron oxide nanoaggregates. *Angew. Chem. Int. Ed.* **61**, e202212013 (2022).
12. Cao, F. et al. Artificial-enzymes-armed Bifidobacterium longum probiotics for alleviating intestinal inflammation and microbiota dysbiosis. *Nat. Nanotechnol.* **18**, 617–627 (2023).
13. Su, J. et al. Single-site iron-anchored amyloid hydrogels as catalytic platforms for alcohol detoxification. *Nat. Nanotechnol.* **19**, 1168–1177 (2024).
14. Huang, C. et al. Hydrogen-bonded organic framework-based bioorthogonal catalysis prevents drug metabolic inactivation. *Nat. Catal.* **6**, 729–739 (2023).
15. Wang, D. et al. Self-assembled single-atom nanozyme for enhanced photodynamic therapy treatment of tumor. *Nat. Commun.* **11**, 357 (2020).
16. Xu, Y. et al. The Fe-N-C nanozyme with both accelerated and inhibited biocatalytic activities capable of accessing drug–drug interactions. *Angew. Chem. Int. Ed.* **59**, 14498–14503 (2020).
17. Wu, W. et al. Reversible inhibition of the oxidase-like activity of Fe single-atom nanozymes for drug detection. *Chem. Sci.* **13**, 4566–4572 (2022).
18. Broto, M. et al. Nanozyme-catalysed CRISPR assay for preamplification-free detection of non-coding RNAs. *Nat. Nanotechnol.* **17**, 1120–1126 (2022).
19. Jiao, L. et al. When nanozymes meet single-atom catalysis. *Angew. Chem. Int. Ed.* **59**, 2565–2576 (2020).
20. Wu, Y. et al. Harmonizing enzyme-like cofactors to boost nanozyme catalysis. *Angew. Chem. Int. Ed.* **63**, e202319108 (2024).
21. Wang, Y. et al. Spatial engineering of single-atom Fe adjacent to Cu-assisted nanozymes for biomimetic O_2 activation. *Nat. Commun.* **15**, 2239 (2024).
22. Huang, L., Chen, J., Gan, L., Wang, J. & Dong, S. Single-atom nanozymes. *Sci. Adv.* **5**, eaav5490 (2019).
23. Zhao, Q. et al. Rearranging spin electrons by axial-ligand-induced orbital splitting to regulate enzymatic activity of single-atom nanozyme with destructive d–π conjugation. *J. Am. Chem. Soc.* **146**, 14875–14888 (2024).
24. Ji, S. et al. Matching the kinetics of natural enzymes with a single-atom iron nanozyme. *Nat. Catal.* **4**, 407–417 (2021).
25. Xu, W. et al. Atomic-level design of metalloenzyme-like active pockets in metal–organic frameworks for bioinspired catalysis. *Chem. Soc. Rev.* **53**, 137–162 (2024).
26. Lan, G. et al. Biomimetic active sites on monolayered metal–organic frameworks for artificial photosynthesis. *Nat. Catal.* **5**, 1006–1018 (2022).
27. Li, G. et al. Dimensionality engineering of single-atom nanozyme for efficient peroxidase-mimicking. *J. Am. Chem. Soc.* **145**, 16835–16842 (2023).
28. Mirts, E. N., Bhagi-Damodaran, A. & Lu, Y. Understanding and modulating metalloenzymes with unnatural amino acids, non-native metal ions, and non-native metallocofactors. *Acc. Chem. Res.* **52**, 935–944 (2019).
29. Wu, Y. et al. Cascade reaction system integrating single-atom nanozymes with abundant Cu sites for enhanced biosensing. *Anal. Chem.* **92**, 3373–3379 (2020).
30. Zhou, J. et al. Coordination-driven self-assembly strategy-activated Cu single-atom nanozymes for catalytic tumor-specific therapy. *J. Am. Chem. Soc.* **145**, 4279–4293 (2023).
31. Xu, W. et al. Photoexcited Ru single-atomic sites for efficient biomimetic redox catalysis. *Proc. Natl. Acad. Sci. USA* **120**, e2220315120 (2023).
32. Zeng, R. et al. Precise tuning of the D-band center of dual-atomic enzymes for catalytic therapy. *J. Am. Chem. Soc.* **146**, 10023–10031 (2024).

33. Cong, Y. et al. Protein Corona-mediated inhibition of nanozyme activity: impact of protein shape. *J. Am. Chem. Soc.* **146**, 10478–10488 (2024).
34. Nayak, S., McPherson, I. J. & Vincent, K. A. Adsorbed intermediates in oxygen reduction on platinum nanoparticles observed by in situ IR spectroscopy. *Angew. Chem. Int. Ed.* **57**, 12855–12858 (2018).
35. Woertink, J. S. et al. A $[Cu_2O]^{2+}$ core in Cu-ZSM-5, the active site in the oxidation of methane to methanol. *Proc. Natl. Acad. Sci. USA* **106**, 18908–18913 (2009).
36. Zhang, H. et al. Hydrogen-bond bridged water oxidation on {001} surfaces of anatase TiO_2. *J. Phys. Chem. C.* **121**, 2251–2257 (2017).
37. Wang, B., Zhang, X., Fang, W., Rovira, C. & Shaik, S. How do metalloproteins tame the Fenton reaction and utilize •OH radicals in constructive manners? *Acc. Chem. Res.* **55**, 2280–2290 (2022).
38. Wu, Y. et al. Oxidase-like Fe-N-C single-atom nanozymes for the detection of acetylcholinesterase activity. *Small* **15**, 1903108 (2019).
39. Wang, X., Qin, L., Zhou, M., Lou, Z. & Wei, H. Nanozyme sensor arrays for detecting versatile analytes from small molecules to proteins and cells. *Anal. Chem.* **90**, 11696–11702 (2018).
40. Isaia, F. et al. Interaction of methimazole with I_2: X-ray crystal structure of the charge transfer complex methimazole–I_2. Implications for the mechanism of action of methimazole-based antithyroid drugs. *J. Med. Chem.* **51**, 4050–4053 (2008).
41. Manna, D., Roy, G. & Mugesh, G. Antithyroid drugs and their analogues: synthesis, structure, and mechanism of action. *Acc. Chem. Res.* **46**, 2706–2715 (2013).
42. Chen, X., Zhou, Y., Peng, X. & Yoon, J. Fluorescent and colorimetric probes for detection of thiols. *Chem. Soc. Rev.* **39**, 2120–2135 (2010).
43. Ochs, R. S. Understanding enzyme inhibition. *J. Chem. Educ.* **77**, 1453 (2000).
44. Paulsen, C. E. & Carroll, K. S. Cysteine-mediated redox signaling: chemistry, biology, and tools for discovery. *Chem. Rev.* **113**, 4633–4679 (2013).
45. Roth, L., Gotsbacher, M. P. & Codd, R. Immobilized metal affinity chromatography as a drug discovery platform for metalloenzyme inhibitors. *J. Med. Chem.* **63**, 12116–12127 (2020).
46. Bhuyan, B. & Mugesh, G. Heme peroxidase-catalyzed iodination of human angiotensins and the effect of iodination on angiotensin converting enzyme activity. *Inorg. Chem.* **47**, 6569–6571 (2008).
47. Delley, B. From molecules to solids with the $DMol^3$ approach. *J. Chem. Phys.* **113**, 7756–7764 (2000).
48. Perdew, J. P., Burke, K. & Ernzerhof, M. Generalized gradient approximation made simple. *Phys. Rev. Lett.* **77**, 3865–3868 (1996).
49. Grimme, S. Semiempirical GGA-type density functional constructed with a long-range dispersion correction. *J. Comput. Chem.* **27**, 1787–1799 (2006).
50. Li, J. Second coordination sphere regulates nanozyme inhibition to assist early drug discovery. *Zenodo* https://doi.org/10.5281/zenodo.15003366 (2025).

Acknowledgements

The authors gratefully acknowledge the financial support from the Fundamental Research Funds for the Central Universities (nos. CCNU22JC006 and CCNU24JCPT032) (C.Z.), and the Program of Introducing Talents of Discipline to Universities of China (111 program, B17019) (C.Z.). The authors thank the support of 1W1B beamline at Beijing Synchrotron Radiation Facility for the XAFS experiments.

Author contributions

C.Z. supervised the research. Y.W. and C.Z. conceived the idea and designed experiments. Y.W. and J.L. conducted most of the experiments and data analysis. W.J., W.X., and W.G. provided technical advice and result interpretation. Y.W. and C.W. contribute to theoretical calculations. L.Z. conducted the XAS experiments. Y.W. and C.Z. wrote the manuscript and supplementary information, and all the authors commented on and amended both documents. All the authors discussed and contributed to the work.

Competing interests

The authors declare no competing interests.

Additional information

Supplementary information The online version contains supplementary material available at https://doi.org/10.1038/s41467-025-58291-7.

Correspondence and requests for materials should be addressed to Chengzhou Zhu.

Peer review information *Nature Communications* thanks the anonymous reviewer(s) for their contribution to the peer review of this work. A peer review file is available.